Materials Research. 2025; 28: e20250165
DOI: https://doi.org/10.1590/1980-5373-MR-2025-0165

The Microstructure, Tensile Properties and Corrosion Resistance of Mg–Al–Sn–Zn Alloys Modified by Minor Ce Addition

***Guojun Liu*[a], *LiPing Liu*[b], *Feng Li*[c], *Yue Wang*[c], *Jiasheng He*[c],**

ChenYe Yu*[a], *Sheng Guan*[a], *Ting Wang*[a]

[a]*Jilin University, Key Laboratory of Automobile Materials of Ministry of Education & School of Materials Science and Engineering, Nanling Campus, No. 5988 Renmin Street, 130025, Changchun, China.*
[b]*Jilin University, International Center of Future Science, No. 2699 Qianjin Street, 130012, Changchun, China.*
[c]*FAW FOUNDRY CO., LTD., Crossing of Hexie Street & Bingwu Road, 130013, Changchun, China.*

Received: January 20, 2025; Revised: June 10, 2025; Accepted: June 23, 2025

The microstructures, tensile properties and corrosion resistance of Mg–7.5Al–2Sn–1Zn (ATZ721) base alloys modified by minor cerium (Ce) additions (0.5, 1.0 and 2.0 wt. %) were investigated. Ce addition leads to the formation of Al_4Ce phase, reduces volume fraction of $Mg_{17}Al_{12}$ phase and refines the microstructures. Tensile tests demonstrated that Ce significantly improved the mechanical properties at room temperature (RT) and 175°C. The alloy with 1.0 wt.% Ce showed superior performance with an ultimate tensile strength (UTS) of 237 MPa, yield strength (YS) of 98 MPa and elongation to failure (E_f) of 16.7% at RT, representing 22%, 17% and 52% improvements over the base alloy, respectively. Corrosion resistance was notably enhanced, with the 1.0 wt.% Ce alloy exhibiting a corrosion rate of 1.8 mm/yr in a 3.5 wt.% NaCl solution, significantly lower than the base alloy's 8.4 mm/yr.

Keywords: *Mg–Al–Sn–Zn, Ce, tensile properties, corrosion resistance, Al_4Ce.*

1. Introduction

The urgent challenge of global warming underscores the necessity for innovative strategies aimed at enhancing energy efficiency in transportation[1-4]. Key strategies include reducing vehicle weight and adopting sustainable materials that offer significant cost savings. Magnesium (Mg) alloys, recognized as the lightest structural metals, stand out for their low density and higher recyclability compared to Al alloys or steel[2]. Mg-Al series Mg alloys comprise a significant portion of commercial Mg alloys[3]. However, their application is limited by the insufficient strength at elevated temperatures and poor corrosion resistance[1,5]. Thus, improving these characteristics is crucial for broader use.

Recently, Mg-Al-Sn-Zn (ATZ) base alloys have emerged as promising candidates, benefiting from the advantageous properties of both Sn and Zn in Mg applications[6-8]. Sn contributes to solid solution strengthening and the formation of Mg_2Sn precipitates, while even small amounts of Zn refine these precipitates, improving ductility[9]. Research on ATZ-base alloys predominantly focuses on low-Al contents, with studies on high-Al contents above 6 wt. % being relatively scarce[10,11]. Liu et al.[11] reported that introducing 3 wt.% Zn enhanced the strength of Mg-9Al-6Sn (wt.%) alloys owing to the refined Mg_2Sn and $Mg_{17}Al_{12}$ phases, while excessive Zn deteriorates corrosion resistance. Ma et al.[12] revealed that 1 wt. % Zn addition enhances the strength and ductility of Mg-8Al-2Sn (wt.%) alloys at room temperature owing to the refined microstructures. However, the improvement at 175°C is limited by the low-melting coarse $Mg_{17}Al_{12}$ phases along the grain boundaries.

Modifying alloy microstructure can significantly enhance mechanical properties and corrosion resistance[3,6]. Alloying has been proved to be an effective method to modify the microstructures in Mg alloys[12-18]. Cerium (Ce) element emerges as a preferable choice for Mg-Al alloys, which is lighter and more affordable than some RE elements (Nd, Y and Gd)[17]. Ce integration leads to the formation of Al-Ce phases ($Al_{11}Ce_3$, Al_4Ce and Al_2Ce), which refine the microstructure, replacing less desirable $Mg_{17}Al_{12}$ phase, thus enhancing mechanical properties[16-18]. Optimal concentrations of Ce not only refine the microstructure of alloys like AZ91 and AM60 but also introduce thermally stable Al-Ce phases, replacing the lower-melting $Mg_{17}Al_{12}$ phase during solidification, thereby enhancing mechanical properties[17,18]. Kim et al.[19] identified that a 1 wt.% Ce addition could significantly refine the grain size of α-Mg in as-cast Mg-4Al-2Sn-1Ca (wt.%) alloy, substantially improving its tensile properties. Another study shows that 0.4 wt.% Ce in AZ31 refines α-Mg, improving the mechanical performance through heterogeneous nucleation of α-Mg on Al_4Ce phase during solidification[20]. Despite these findings, studies on Ce effects on Mg-Al-Sn-Zn alloys with high-Al concentration remain scare.

Corrosion resistance is a crucial consideration for Mg alloys due to the low electrochemical potential of pure Mg[21-26]. Research on Ce-containing Mg-Al alloys, such as AM60, AZ91 and AT42, reveals that optimal Ce levels significantly improve corrosion resistance in NaCl solutions[18,26]. The

*e-mail: wanting@jlu.edu.cn
Associate Editor: José Daniel Biasoli de Mello.
Editor-in-Chief: Luiz Antonio Pessan.

improvement is attributed to Ce distribution within the passive film and refined microstructures with reduced $Mg_{17}Al_{12}$ phase fraction, minimizing micro-galvanic corrosion between secondary phases and α-Mg[3,24]. However, excessive Ce has the opposite effect, highlighting the importance of optimal Ce concentration, which varies across alloys and manufacturing methods[23,25]. Therefore, the influence of Ce on the mechanical and corrosion properties of Mg-Al-Sn-Zn alloys requires further exploration. This study aims to address the gaps in understanding how minor Ce additions influence the Mg-Al-Sn-Zn alloys, focusing on potential benefits or drawbacks regarding the mechanical properties and corrosion resistance in order to expand the applications of Mg alloys.

2. Experimental Methods and Procedure

2.1. Materials preparation

Mg-7.5Al-2Sn-1Zn-0.2Mn (wt. %, the same unit is used hereafter) alloys with free and *x*Ce (*x*: 0.5, 1.0 and 2.0 wt. %) alloys, designed as 1#, 2#, 3# and 4#, respectively, were prepared from pure Mg (99.9%), Al (99.9%), Sn (99.9%), Zn (99.9%) and master alloys of Mg-22%Ce and Mg-3%Mn. The fabrication employed a low-carbon steel crucible under the protection of CO_2 and SF_6 at the flow rate ~ 100: 1 in an electric-resistance furnace. The melt was poured into the preheated (~ 200 °C) grey iron mold and obtained ingots. The actual chemical components of ingots were verified by a Sequential X-ray Fluorescence Spectrometer (Shimadzu XRF-1800) and the results were listed in Table 1. To evaluate the grain size of α-Mg, select samples were subjected to a heat treatment. This involved an initial solid solution treatment at 415 °C for 20 h, followed by a gradual temperature increase to 480 °C at a rate of 2 °C/min. The samples were held at this temperature for 2 h within a resistance furnace under a high-purity argon atmosphere before being quenched in water. For metallographic observation, the as-cast specimens were etched by the mixed solution of 2 ml HNO_3 and 48 ml C_2H_5OH for 10~15s, while the solid solution samples were etched by the mixed solution consisting of 2.1 g picric acid, 5 mL acetic acid and 5 mL distilled water in 40 mL ethanol.

2.2. Tensile tests

Tensile testing was conducted using at least three specimens on a universal mechanical tester (Instron 5869, USA) at room temperature (RT) and 175 °C, with a strain rate of $1.0\times10^{-3}s^{-1}$. The samples were holding for 10 min at 175 °C prior to testing at 175 °C. The dogbone tensile specimens have a nominal width of 4 mm, a gauge length of 10 mm, and a thickness of 2 mm.

2.3. Immersion and electrochemical measurements

The 10 mm × 10 mm × 10 mm specimens were cut from ingots and ground to a 2000 grit finish for each surface follow by ultrasonic cleaning in distilled water, ethanol, acetone in turn, then dried in air. The changed weight of samples before and after immersion tests was measured by an electronic balance (HXD-1000, PE, USA) with sensitivity of 0.0001 mg. Next, the sample was placed in a pyrex glass beaker and a calibrated hydrogen collection tube set up over the surface of the corroding sample where is filled with 3.5 wt. % NaCl solution at 25°C[17]. The corrosion rate was determined base on the hydrogen evolution method, as outlined by Song and Atrens[27], with hydrogen volume recorded at specific time intervals ranging from the onset up to 96 h. After immersion, some samples were cleaned in the boiling mixed solution of CrO_3 (200 g/L) and $AgNO_3$ (10 g/L) to remove the corrosion product for measuring the weight again for subsequent corrosion rate calculations and microstructural examination.

The preparation of samples for electrochemical polarization tests involves selecting one working surface of 1 cm^2 and sealing the other surfaces, including a Cu line at the opposite side of the working face, in epoxy resin. This process ensures that the working surface can conduct electricity while the other surfaces are electrically isolated. The work surface was then ground to a 3000-grit finish surface follow by ultrasonic cleaning in distilled water, ethanol, acetone and dry in air in turn. Electrochemical evaluations were conducted using a three-electrode cell in an electrochemical workstation (PARSTAT3000A-DX, Princeton, Ametek, Slovakia) with a saturated calomel electrode (SCE) as the reference, a large-area platinum electrode as the counter, and the sample as the working electrode. All tests were performed in a 3.5 wt. % NaCl solution at a stable temperature of 25 °C. The open-circuit potential (OCP) was monitored for 60 min to stabilize before measurements. The OCP of the samples was in 3.5 wt. % NaCl solution in the range of -1.58 to -1.56V. The electrochemical impedance spectroscopy (EIS) measurements were conducted under the stable OCP after an initial delay of 60 min immersion, over the frequency range of 10^5 to 10^{-2} Hz, and the EIS data were fitted by Zview 3.3 software to propose the equivalent electrical circuits to analyze the experiment data. Polarization curves were traced from -2.0 V to -1.1 V at a scan rate of 0.5 mV/s. The corrosion potential (E_{corr} vs. SCE, V) and the corrosion current density (i_{corr}, A/cm^2) were calculated according to the polarization curves. Each measurement was repeated at least twice to ensure reproducibility of the results.

2.4. Materials characterization

The metallographic microstructures of solid-solution treated samples were thoroughly examined using an optical microscope (OM, Zeiss, Axio Imager.A2m, Germany). The

Table 1. The actual chemical composition of the experimental alloys (wt.%).

Alloy	Al	Sn	Zn	Mn	Ce	Mg
1#	7.623	2.883	1.081	0.171	0	Bal.
2#	7.515	2.879	1.056	0.165	0.381	Bal.
3#	7.584	2.914	1.028	0.168	0.789	Bal.
4#	7.524	2.935	1.077	0.166	1.762	Bal.

microstructures, tensile fractures and corrosion morphologies, as well as the distribution of alloying elements and phases, were conducted using a scanning electron microscope (SEM, Zeiss, VOA-18, Germany) equipped with an energy dispersive spectrometer (EDS, INCA-X-Max, England). Phase identification in both as-cast and non-cleaned immersed specimens was achieved through X-ray diffraction (XRD, DX-2700B, HaoYuan, China), utilizing filtered Cu K_α radiation at settings of 40 kV and 40 mA. Macroscopic changes after 96 h of immersion, followed by cleaning, were observed under a stereo microscope to assess any significant morphological changes. The average grain size in the solid solution treated samples was accurately measured using NanoMeasurer 3.0 software[28]. Furthermore, to provide an in-depth characterization of secondary phases and their elemental distribution, transmission electron microscopy (TEM, JEM-2100F, Japan) with EDS offering high-resolution insights into the microstructural features.

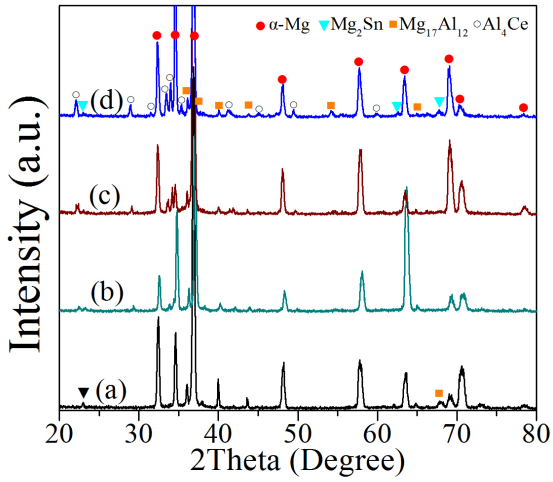

Figure 1. XRD patterns of as-cast alloys. (a) 1#; (b) 2#; (c) 3# and (d) 4#.

3. Results and Discussion

3.1. Phase and microstructure of as-cast alloys

Figure 1 illustrates the XRD patterns of as-cast alloys. As evidenced in Figure 1(a), 1# alloy is composed of α-Mg, $Mg_{17}Al_{12}$ (β) and Mg_2Sn (γ) phases. The addition of Ce caused the formation of new phase of Al_4Ce (Figures 1b-d), which is similar to AM60 and AZ61 alloys with Ce addition[29,30]. Moreover, with the increasing of Ce, the intensity of the Al_4Ce phase increases, but results in a corresponding decrease in the intensity of the $Mg_{17}Al_{12}$ phase. Additionally, the addition of Ce appears to have minimal impact on Mg_2Sn phase, which remains relatively consistent across varying levels of Ce addition. Note that, there is no Al_2Ce or $Al_{11}Ce_3$ phases as reported in die-cast AE44 alloys, possibly related to the varying concentration of Ce in alloys and the fabrication processes[16].

Figure 2 provides the optical images of solid solution treated samples and corresponding grain size distribution of α-Mg. It can be seen that with the increasing of Ce, the average grain size of α-Mg initially decreases then slightly increases, indicating this grain refinement effect weakens when Ce addition exceeds an optimal level. Notably, 3# alloy with 1.0 wt.% Ce addition exhibits the finest average grain size in α-Mg of ~140 μm.

Figure 3 presents the typical SEM graphs of as-cast samples. The microstructure of 1# alloy is predominantly composed of eutectic α-Mg (α), primary α-Mg (α'), eutectic β-$Mg_{17}Al_{12}$ (β), secondary precipitation β-$Mg_{17}Al_{12}$ (β') and eutectic Mg_2Sn (γ) as shown in Figure 3(a). The bony-like β phase is surrounded with eutectic α-Mg, suggesting that the reaction of α-Mg + Al → β-$Mg_{17}Al_{12}$ is divorced eutectic reaction[6]. Additionally, a fine, flaky distribution of β' phase near the β phase is observed, along with sporadic divorced γ phases indicated by arrows in Figure 4a. Upon the addition of 0.5 wt.% Ce into the alloy, a few new, rod-like Al_4Ce phases emerge along the grain boundaries and within the grains. As the Ce concentration surpasses 0.5 wt.%, a marked reduction in the β phase fraction occurs, accompanied by a morphological changing from bone-like and semi-continuous

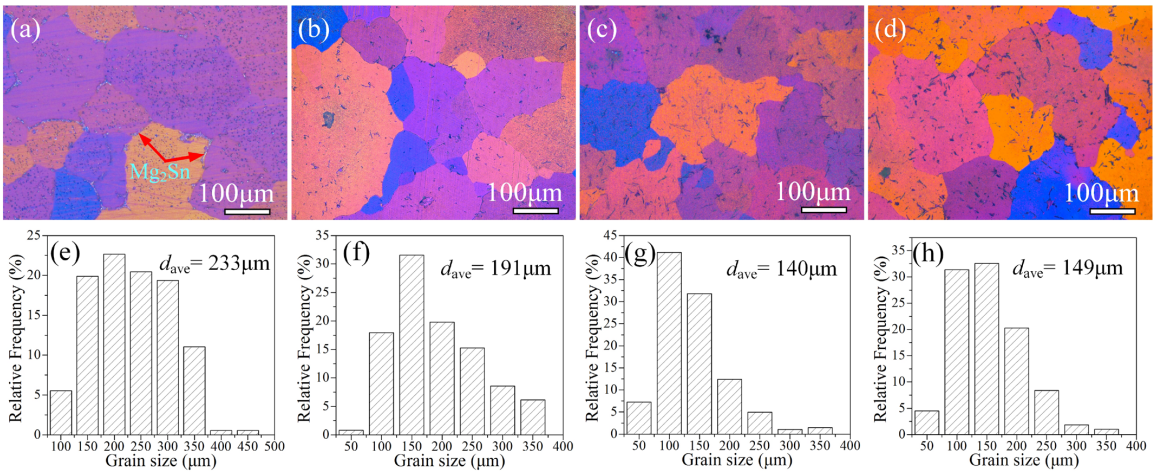

Figure 2. Optical graphs of solid solution treated samples for (a) 1#, (b) 2#, (c) 3# and (d) 4#, and the corresponding grain size distribution for (e) 1#, (f) 2#, (g) 3# and (h) 4#, respectively.

to particulate (Figures 3a, 3e and 4a). Simultaneously, the fraction of Al_4Ce phase increases (Figures 3e-h), and its morphology changes from short needle-like to coarse-rod- or large block-like along the grain boundaries and within the grains (Figures 3 and 4). This suggests that small amounts of Ce additions refine the $Mg_{17}Al_{12}$ phase and promote the formation of the Al_4Ce phase, consistent with findings in Ce-containing Mg-Al alloys[17].

Moreover, the addition of Ce leads to a gradual reduction in the size of the Mg_2Sn (γ) phase (Figures 3a, d, h and Figure 4), likely due to the refined β phase. The results from the EDS points scan (Figure 4i) suggest that the intermetallic

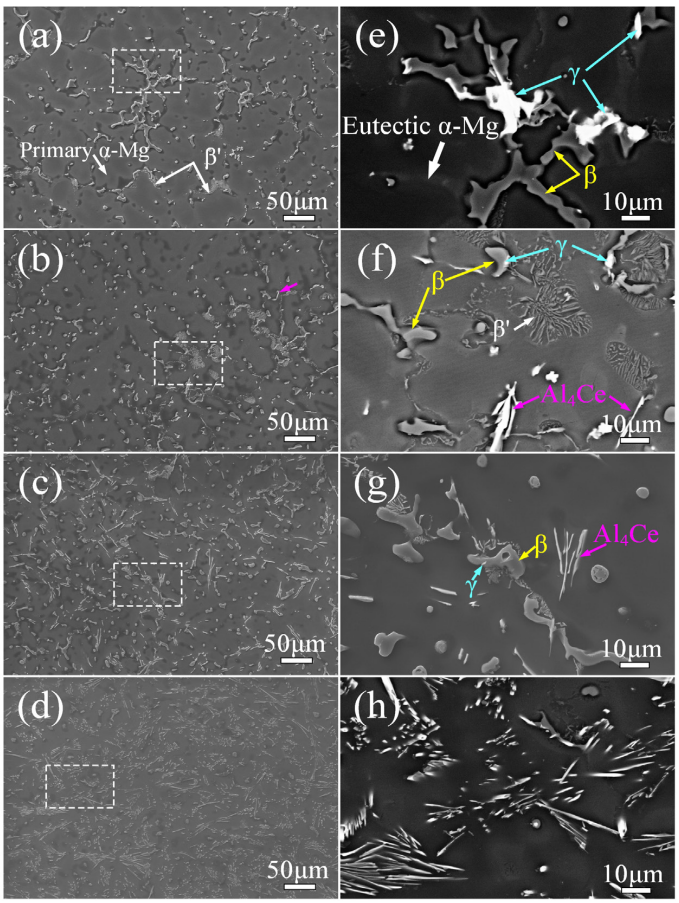

Figure 3. SEM microstructures of as-cast alloys: (a), (e) 1#; (b), (f) 2#; (c), (g) 3# and (d), (h) 4#. Note that (b), (d), (f) and (h) are the high magnification of local regions as pointed by dotted rectangles in (a), (c), (e) and (g) respectively.

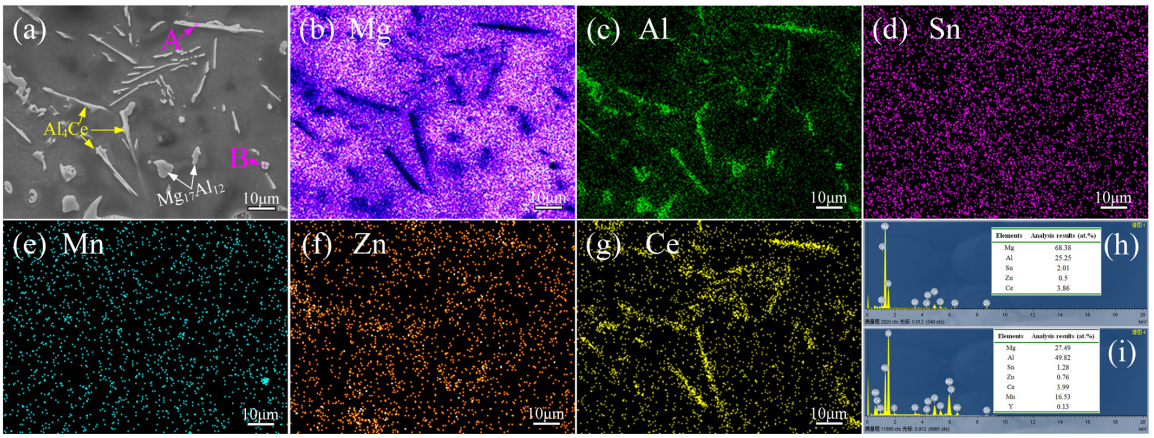

Figure 4. Surface morphology (a) of 3# alloy and EDS results of mapping (b-g) and points (h, i) on (a). (h) and (i) are point scanning of Point A and B in (a) with the inserted images.

compound at point "B" in Figure 4a is possibly $Al_{10}Ce_2Mn_7$, base on the atomic ratio[15]. Figure 5 presents TEM results of the 3# alloy. STEM analysis further reveals a complex microstructure that the Mg_2Sn and Al_4Ce phases exhibit interdependent growth showing. The rod-like Al_4Ce phase is approximately 4.5 μm in length, whereas Mg_2Sn phase extends to about 0.6 μm. These fine secondary phases are helpful to enhance the mechanical properties of the alloys.

3.2. Tensile properties and fracture morphology

Figure 6 depicts the typical engineering stress-strain curves of samples at room temperature (RT, Figure 6a) and 175 °C (Figure 6b) and presents a comparison of the tensile properties of Mg alloys in this work with relevant Mg alloys at RT (Figure 6c)[31-39] and 175°C (d)[31,36-38,40-42]. The average tensile properties are summarized in Table 2. A small addition of Ce evidently enhances the ultimate tensile strength (UTS), yield strength (YS) and elongation to failure (E_f) of the base alloy. As the Ce additions increase, both UTS and YS increase, while E_f decreases. A comparison between 3# and 4# alloys reveals that 4# exhibits marginally higher strength but significantly lower ductility (Table 2). Consequently, 3# alloy exhibits outstanding tensile properties, with average UTS, YS and E_f of approximately 237 MPa, 98 MPa and 16.7% at RT, representing improvements of about 22%, 17%, and 52%, respectively, compared to the base alloy. Similarly, at 175 °C, 3# alloy maintains superior tensile properties, with average UTS, YS and E_f of approximately 146 MPa, 85 MPa and 27.7%, respectively. These values correspond to improvements of 11%, 15% and 45%, respectively, over the base alloy. In addition, the tensile properties

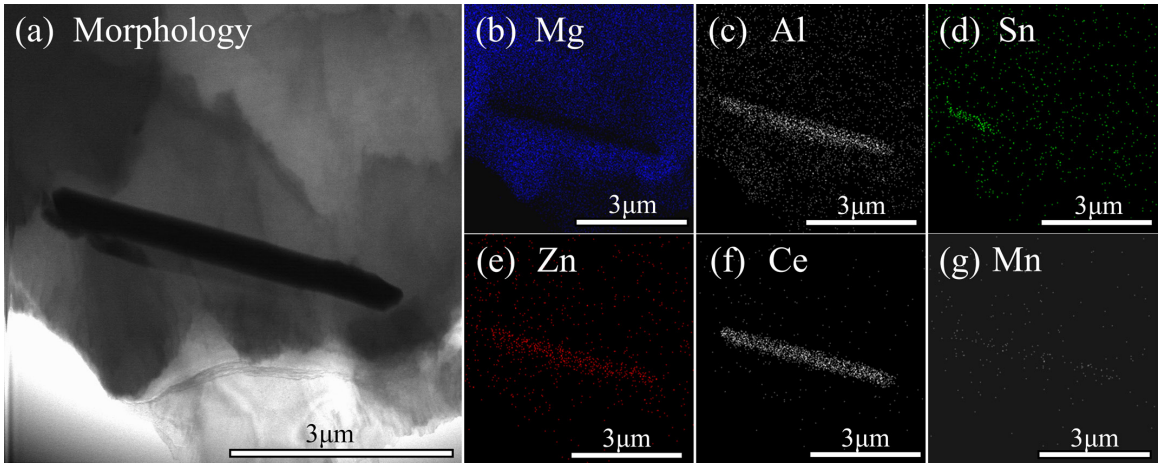

Figure 5. TEM microstructure (a) and the distribution of elements by STEM (b-g) on 3# alloy.

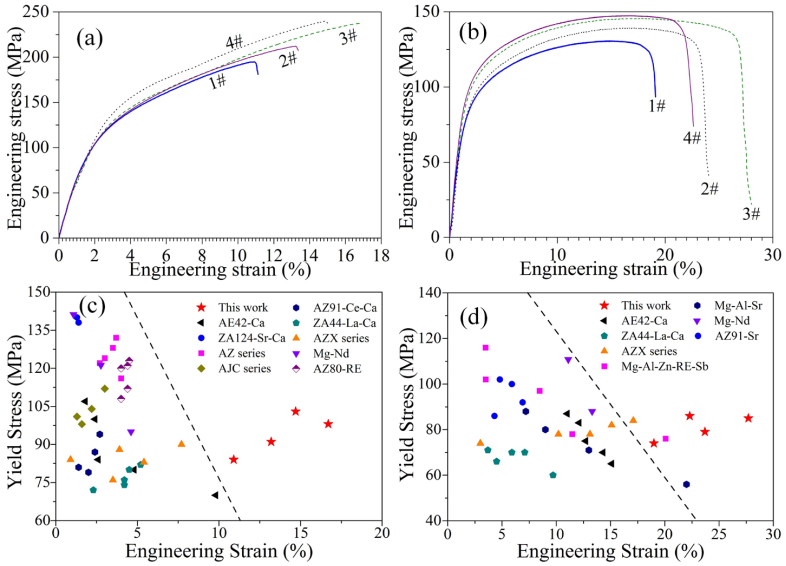

Figure 6. The engineering stress-strain curves of as-cast samples at RT (a) and 175°C (b). Moreover, a comparison of the tensile properties of this work with relevant Mg alloys is presented at RT (c)[31-39] and 175°C (d)[31,36-38,40-42].

of studied alloys were compared with those of other Mg alloys fabricated by the same casting method[31-42]. At RT (Figure 6c), the AZ series Mg alloys[33], Mg-Nd alloys[38] and ZA124-Sr-Ca alloy[32] exhibit relatively high YS. However, their elongation is less than 5%, which implies poor plasticity. Similarly, at 175 °C, Mg-Al-Zn-RE-Sb alloy[41] displays a high YS, yet its elongation is only around 15%, indicating limited plasticity. Overall, when balancing the YS and ductility, Mg-7.5Al-2Sn-1Zn-0.2Mn-1.0Ce alloy (i.e., 3# alloy), demonstrates excellent comprehensive performance in terms of strength and ductility.

Figure 7 illustrates the typical tensile fractures of as-cast samples tested at RT and 175°C. At RT, the presence of discontinuous cracks and small cleavage steps on the fractures suggests that the fracture modes are a combination of cleavage and quasi-cleavage fracture modes[5]. In contrast,

Table 2. The average values of tensile properties for as-cast alloys at RT and 175°C.

Alloy	RT			175°C		
	UTS(MPa)	YS(MPa)	E_f(%)	UTS(MPa)	YS(MPa)	E_f(%)
1#	196^{+3}_{-2}	84^{+2}_{-1}	$10.9^{+0.2}_{-0.3}$	131^{+2}_{-3}	74^{+2}_{-1}	$19.0^{+0.1}_{-0.4}$
2#	215^{+2}_{-3}	91^{+2}_{-2}	$13.2^{+0.3}_{-0.8}$	139^{+4}_{-2}	79^{+3}_{-2}	$23.7^{+0.3}_{-0.5}$
3#	237^{+1}_{-6}	98^{+4}_{-3}	$16.7^{+0.3}_{-0.4}$	146^{+3}_{-1}	85^{+2}_{-3}	$27.7^{+0.4}_{-0.5}$
4#	239^{+3}_{-2}	103^{+5}_{-3}	$14.7^{+0.4}_{-1.2}$	148^{+4}_{-2}	86^{+1}_{-2}	$22.3^{+0.7}_{-0.1}$

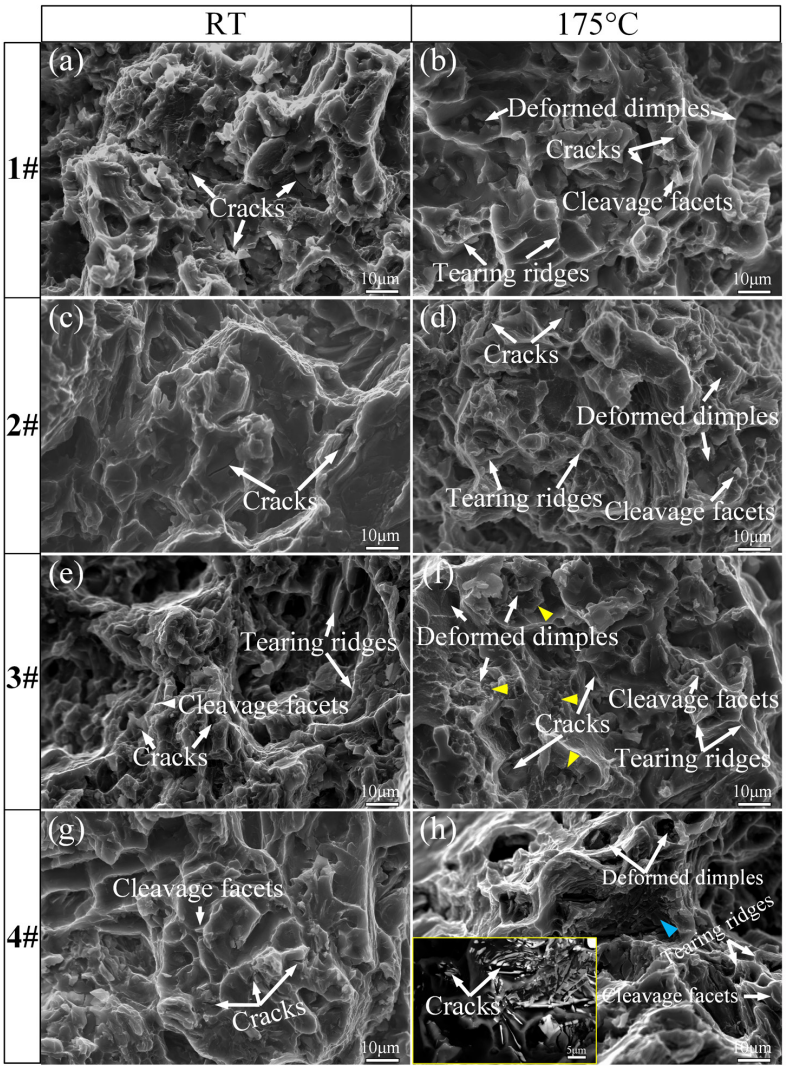

Figure 7. SEM fractures of tensile samples tested at RT and 175°C. The insert in (h) is a high- magnification view of local region in (h) as pointed by blue arrow.

at 175°C, the appearance of deformed dimples, small cracks, tearing ridges and cleavage facets on the surfaces (Figures 7b, d, f and g) indicates that quasi-cleavage fracture predominates the fracture mode. The addition of Ce does not significantly alter the fracture characteristics at a given temperature. However, excessive addition of Ce leads to the coarsening of the Al_4Ce phase (Figure 3d and the insert in Figure 7h), which tends to initiate cracks, thereby decreasing the tensile strength and elongation of the alloy. Thus, it is inferred that the abundant Al_4Ce phase adversely affects the plastic deformation of 4# alloy with 2 wt.% Ce addition.

3.3. Corrosion behavior

3.3.1. Immersion test

Figure 8 displays the hydrogen evolution volume of as-cast alloys immersed in 3.5 wt. % NaCl solution at 25°C for 96 h. The volume of hydrogen evolved from 1# alloy exhibits a rapid increases compared to the Ce-containing alloys, indicating that Ce addition effectively inhibits the hydrogen evolution reaction and reduces the corrosion rates of the base alloy. The average corrosion rate was calculated using the Equation (1),

$$C_W = 2.1\Delta m / At \quad (1)$$

where C_w is the corrosion rate in mm/yr, Δm is the mass loss in mg, A is the surface area in cm^2, t is the total immersion time in day[43]. The calculated average corrosion rates are provided in Table 3, showing that the Ce-containing alloys have lower corrosion rates than the base alloy, indicating that Ce addition enhances the corrosion resistance of the base alloy. Notably, the alloy with 1.0 wt.% Ce exhibits the highest corrosion resistance, with a corrosion rate of 1.6 mm/yr, significantly lower than 14.4 mm/yr observed in the base alloy. Consequently, the corrosion resistance base on the immersion tests is following the order 3# > 2# > 4# > 1# alloy.

3.3.2. Electrochemical measurements

Figure 9 shows the polarization curves of samples in a 3.5 wt.% NaCl solution at 25°C and the corrosion current densities (i_{corr}) and corrosion potentials (E_{corr}) are calculated as shown in Table 3. The addition of Ce causes the polarization curves to shift towards i_{corr} and less negative E_{corr} compared to the base alloy, aligning with AM60-Ce alloys[18]. Furthermore, the cathodic branches of the Ce-containing alloys are positioned lower, indicating that hydrogen evolution is inhibited. The anodic curves for base alloy appear to reach the limiting current almost immediately, whereas those for the Ce-containing alloys change more gradually near the stable potential, especially for 2# and 3# alloys, which exhibit a stable step. This indicates a delay in the anodic reaction. The calculated i_{corr} for the Ce-containing alloys decreased by up to an order of magnitude in contrast with the base alloy (Table 3), demonstrating that the addition of Ce effectively hinders the corrosion of the base alloy. Furthermore, the corrosion current density (i_{corr}) obtained

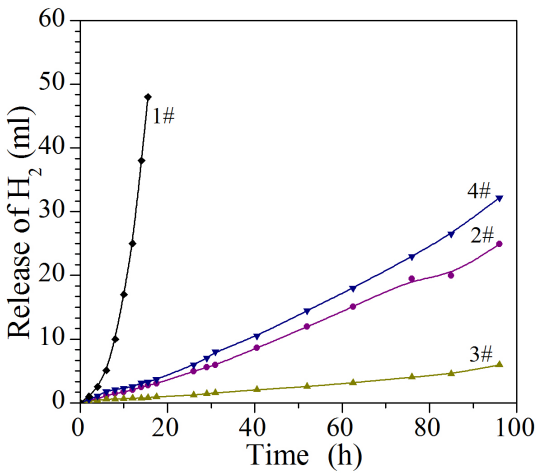

Figure 8. Evolution of H_2 release on as-cast samples during immersing for 96h.

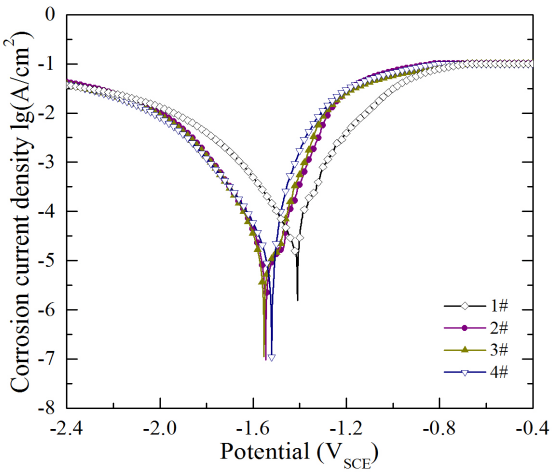

Figure 9. Polarization curves of as-cast samples tested in 3.5 wt.% NaCl solution.

Table 3. The results of the polarization curves of as-cast samples.

Alloy	E_{corr}(V *vs.* SCE)	β_c(mV/dec)	i_{corr}(10^{-4}×A/cm^2)	C_w(mm/yr)
1#	-1.50±0.11	187.1±10.1	1.853±0.06	8.4±0.3
2#	-1.38±0.07	184.7±8.4	0.735±0.03	3.5±0.1
3#	-1.34±0.04	183.5±6.2	0.642±0.02	1.8±0.06
4#	-1.38±0.08	185.0±6.7	1.282±0.03	3.7±0.2

from the polarization curves can be utilized to estimate the transient corrosion rate of the samples using Equation (2)[44]:

$$P_i = 22.85 i_{corr} \quad (2)$$

where P_i is corrosion rate in mm/yr, and i_{corr} is the corrosion current density in mA cm^{-2}. By substituting the i_{corr} values into Equation 2, the corrosion rates of 1#, 2#, 3# and 4# alloy are determined to be 4.234 mm/yr, 1.679 mm/yr, 1.466 mm/yr, and 2.929 mm/yr, respectively. This result suggests that the corrosion-resistance trend of these alloys is consistent with the results of hydrogen evolution (Figure 8) and mass loss (Table 3) obtained from the immersion tests. Among these alloys, 3# alloy exhibits a relatively lower corrosion rate, implying superior corrosion resistance. A comparison reveals that the average corrosion rate calculated by the mass loss method is higher than that obtained from the electrochemical test. This discrepancy can be attributed to factors such as the immersion time of the alloys. During the immersion test, the relatively long immersion time leads to the corrosion of α-Mg, which may cause partial detachment of the second - phase particles. The detachment of these particles increases the surface area available for corrosion, thereby resulting in a slight increase in the average corrosion rate calculated by the mass loss method.

To gain a comprehensive understanding of the corrosion resistance of the studied alloys, the corrosion rates of other as-cast Mg alloys immersed in a 3.5 wt.% NaCl solution, calculated via the mass loss method, were investigated. For instance, the corrosion rates of Mg-3Al-0.03Y alloy[45], Mg-25Al[46], AZ91[47], Mg-5Li-1Al[48], CP Mg[49], and AM50[50] alloys are 5.6 mm/yr, 4.2 mm/yr, 23 mm/yr, 10 mm/yr, 2.7 mm/yr and 5 mm/yr, respectively. Evidently, the corrosion rates of the studied alloys are relatively low, indicating excellent corrosion resistance. It should be pointed out that the differences in corrosion rates are associated with factors such as immersion time, microstructure and the quality of experimental samples, particularly the content of impurities (e.g., Fe, Cu).

Figure 10 shows the EIS spectra for samples in a 3.5 wt.% NaCl solution at 25°C. The Nyquist spectra of the samples (Figure 10a) are composed of a capacitive loop, which is characterized by the constant phase element of the film (CPE_f) and the charge-transfer resistance (R_{ct}) and an inductive loop, represented by the inductance (L) and the inductive resistance (R_L)[51,52]. Herein, CPE_f corresponds to the capacitance of the surface film, while R_{ct} represents the charge - transfer resistance at the electric double-layer interface. Meanwhile, L and R_L denote the inductance and the inductive resistance, respectively. Compared to the base alloy, the capacitive-loop diameter of the Ce-containing alloys is larger, indicating better protective performance of the oxide film formed on the surfaces. Specifically, the alloy with 1.0 wt.% Ce exhibits the largest capacitive loop diameter, accompanied by a greater half-width (Figure 10b)

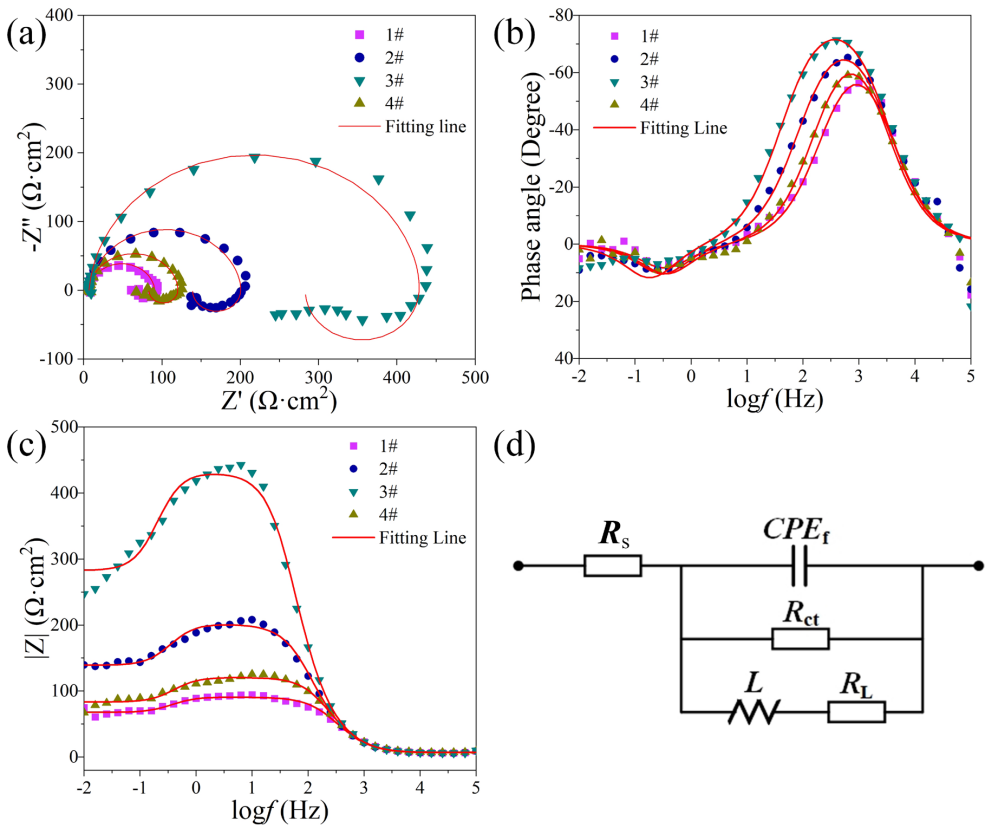

Figure 10. EIS spectra of as-cast samples. (a) Nyquist plots; (b) Bode plots of phase angle with frequency; (c) Bode plots of |Z| with frequency; (d) equivalent circuit for curve-fitting of the EIS results in (a).

and a higher modulus value (Figure 10c), which signifies enhanced corrosion resistance. The EIS spectra of the studied alloys were fitted using the equivalent circuit depicted in Figure 10d, and the detailed fitting data are provided in Table 4. Polarization resistance (R_p) is employed as a key parameter to evaluate the CR of the alloys[50]. Notably, the significantly higher R_p value for the alloy with 1.0 wt.% Ce indicates a lower corrosion rate.

3.3.3. The morphology of corrosion product film

Figure 11 shows XRD patterns of the corrosion product film formed on as-cast alloys after immersion in 3.5 wt.% NaCl solution at 25 °C for 96 h. The base alloy consists primarily of $Mg(OH)_2$, α-Mg and $Mg_{17}Al_{12}$ phases, with $Mg(OH)_2$ exhibiting a stronger intensity compared to the other phases (Figure 11a), indicating its prominence as the predominant surface product[51]. Conversely, in the Ce-added alloys, the intensity of $Mg(OH)_2$ is weaker relative to α-Mg and notable weaker Al_4Ce are observed (Figures 11b-d).

Moreover, corrosion-product surfaces of 1#, 3# and 4# alloys were examined by SEM/BSM with EDS results shown in Figure 12. The surface of 1# alloy is rough with extensive cracks and deep corrosion pits (Figures 12a and d), indicating a uniform predominant corrosion mechanism. The high oxygen content detected on the surface (Figure 12h), coupled with XRD results from Figure 13, suggests that the surface is primarily covered by $Mg(OH)_2$, contrary to the expected Al_2O_3 film in AZ91 alloy[52]. In contrast, the introduction of 1 wt.% Ce significantly reduces both the extent of the corroded area and the depth of corrosion pits (Figures 12b and e), indicating a shift towards localized corrosion as the principal degradation mechanism for the 3# alloy.

Additionally, the appearance of few rod-like Al_4Ce phases on the surface, pointed by red arrows, suggests that these phases act catholically. Increasing the Ce content to 2.0 wt.% in the 4# alloy results in the increased corrosion regions and deeper pits (Figures 12c and f) compared to 3# alloy, although they remain superior to the base alloy. The observation of filiform corrosion in the Ce-containing alloys indicates that localized corrosion continues to be the dominant mechanism. XRD and EDS analyses reveal that the surfaces are largely covered by $Mg(OH)_2$ and Al_4Ce phases (indicated by red arrows). These observations affirm that Ce addition notably alters corrosion behaviors of the base alloy.

Finally, the cleaned surfaces (free of corrosion products) were observed by SLM and SEM, with the identical corrosion characteristics as shown in Figure 13. The surface of 1# alloy prominently featured numerous deep corrosion pits and semi-continuous phases of $Mg_{17}Al_{12}$. In contrast, alloys with Ce additions exhibited reduced corrosion areas, shallow corrosion pits, and residual Al_4Ce phases. These observed secondary phases, which have a relatively high electric potential compared to the α-Mg, acted predominantly as anodic sites during the corrosion process. Consequently, 3# alloy demonstrated improved CR characterized by less corroded regions and shallower corrosion pits, as depicted from a high magnified view in Figure 13i among the studied alloys. The interpretation of varying surface morphologies post-immersion can be attributed to the different electrical potentials of the secondary phases and α-Mg matrix, which will be discussed later.

4. Discussion

4.1. Evolution of microstructures and phase compositions

The addition of Ce significantly modify the as-cast microstructures of the ATZ-base alloy, primarily affecting the evolution of phases and the grain size of α-Mg. According to the alloy composition (Table.1), the substantial electronegativity difference between Al and Ce typically results in the formation of the Al_4Ce phase prior to the α-Mg during solidification processes[18]. Ce, acting as a surface-active element, dramatically decreases the interfacial tension within the alloy during solidification,

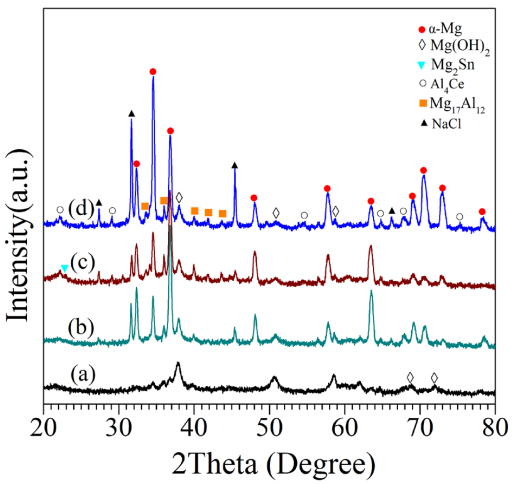

Figure 11. XRD patterns of surfaces (without cleaning) of samples after immersion for 96h.

Table 4. The EIS fitting data of as-cast samples.

Alloys	R_s /Ω·cm²	CPE_f		R_{ct} /Ω·cm²	L /H·cm²	R_L /Ω·cm²	R_p /Ω·cm²
		Y_1/μΩ·cm⁻²·sⁿ	n_1				
1#	6.54	12.28	0.947	84.3	125	222.2	61.11
2#	6.51	13.94	0.938	195.4	254	412.6	132.60
3#	6.87	11.49	0.953	424.5	845	789.7	276.09
4#	7.26	10.72	0.964	113.3	125.4	231.8	76.10

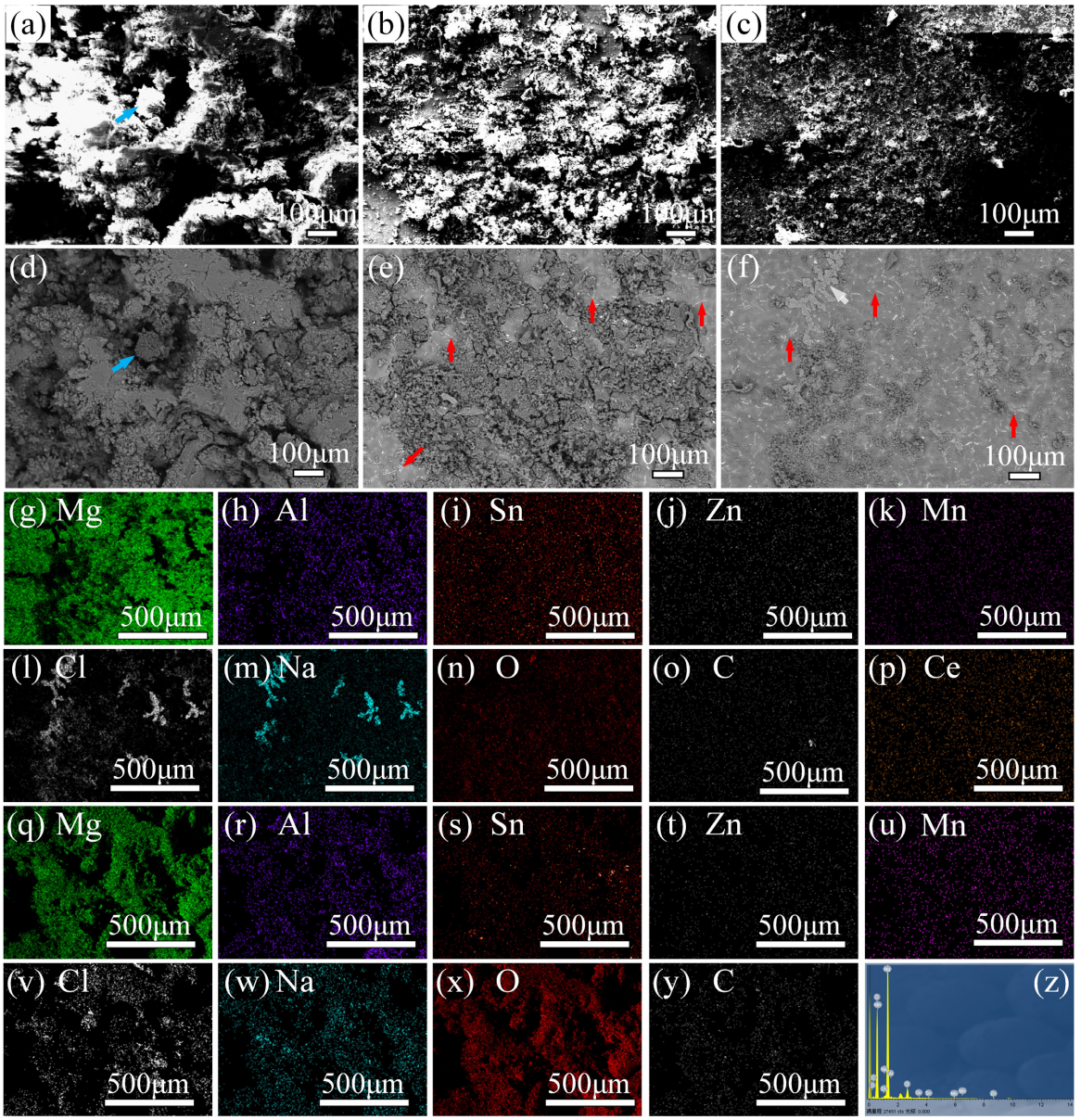

Figure 12. The morphology of surfaces (without cleaning) for 1# (a, d), 2# (b, e) and 3# (c, f) alloys after immersion for 96h. Note that a, b and c are SEM compared to the corresponding BSD of d, e and f respectively. (g–p) are the mapping of 4#, while (n–z) are the mapping and EDS results of 1# alloy.

thereby enhancing the nucleation rate of the α-Mg phase. This enhancement refines the grain size of α-Mg from 233 μm in the base alloy to 140 μm in the 1.0 wt.% Ce-added 3# alloy[53,54]. As α-Mg dendrites grow, the enrichment of Ce at the solidification front due to solute redistribution results in stronger constitutional super cooling. This condition promotes more branched α-Mg structures, which interconnect and divide the remaining melt into numerous isolated small liquid pockets. This isolation restricts the growth of eutectic $Mg_{17}Al_{12}$ and Mg_2Sn phases, aiding in their refinement[55]. Moreover, with Ce addition, the morphology of $Mg_{17}Al_{12}$ change from semi-continuous to more fragmented, net-like structures and discrete particles, likely contributing to improved tensile properties. The addition of Ce also refines the eutectic Mg_2Sn phase, as seen in Figure3. This refinement might be attributed to the high solid solubility of Sn in Mg, influenced by the presence of the Al_4Ce phase. The Al_4Ce phase itself undergoes morphological changes from short rod-like to extended plate-like structures and large dendrites, intensifying with increased Ce levels. These changes are related to Al segregation at local grain boundaries and increased Ce content.

4.2. The effect of Ce addition on the tensile properties

The tensile properties, including UTS, YS and E_f, initially improve but subsequently slightly decline with

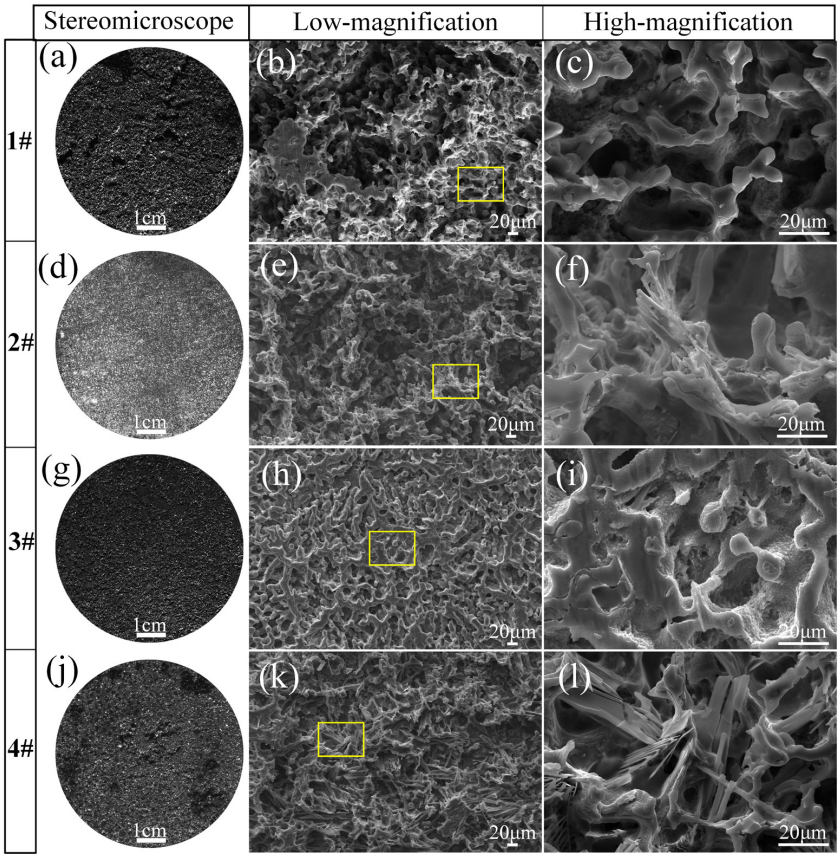

Figure 13. SLM and SEM graphs surfaces of samples immersed in 3.5 wt. % NaCl solution for 96h.

increasing Ce content, attributed to various strengthening mechanisms, such as solid solution strengthening, grain refinement strengthening and secondary phases strengthening. For the solid solution strengthening, alloying elements such as Zn, Al and Sn, which have significant solid solubility in Mg (6.32 wt.% for Zn, 12.62 wt.% for Al and 14.56 wt.% for Sn), enhance solid solution strengthening by hindering dislocation movement[7,8]. In case of grain refinement strengthening, the addition of Ce notably refines the α-Mg grain size from 233 μm in base alloy to 140 μm in 3# alloy (Figure 2). Then, the grain refinement strengthening (σ_{gr}) can be evaluated using Hall-Petch equation: $\sigma_{gr} = k \cdot d^{-1/2}$, in which k is the Hall-Petch coefficient, approximated at 280 MPa·μm$^{1/2}$, and d represents the average grain size of α-Mg[56]. After careful calculation, the σ_{gr} values of base alloy and 3# alloy are 18 MPa and 24 MPa, indicating that YS of 3# alloy was improved approximately 33% compared to the base alloy. Moreover, the introduction of Ce leads to the refinement and more uniform distribution of the $Mg_{17}Al_{12}$ and Mg_2Sn phases, which enhance tensile strength by reducing stress concentration[12]. This is consistent with the principle that finely dispersed precipitates strengthen the material by hindering dislocation motion. However, as Ce content increases, the coarse phases act as stress concentration points, promoting crack initiation and propagation, which adversely affect ductility and tensile strength[15].

4.3. The effect of Ce addition on the corrosion behaviors

Both immersion and electrochemical testing demonstrated that minor Ce addition significantly improved corrosion resistance of base alloy in 3.5 wt.% NaCl solution. Notably, the 3# alloy, containing 1 wt.% Ce, exhibited the lowest corrosion rate. It has been identified that pitting predominantly controls the initial corrosion stages of Mg alloys in NaCl solutions. Initially, a porous MgO layer forms on the alloy surfaces, which gradually reacts with the NaCl solution by the following Equations (3) and (4)[43],

$$MgO + H_2O \rightarrow Mg(OH)_2 \quad (3)$$

$$Mg + 2H_2O \rightarrow Mg(OH)_2 + H_2 \quad (4)$$

where Equation 4 encompass the anodic reaction of $Mg \rightarrow Mg^{2+} + 2e^-$ and cathodic reaction of $2H_2O + 2e^- \rightarrow 2OH^- + H_2$. The formed $Mg(OH)_2$ layer is then dissolved through the reaction as described in Equation (5)[43] due to the aggressiveness of Cl^-, offering limited protection on the Mg matrix.

$$Mg(OH)_2 + 2Cl^- \rightarrow MgCl_2 + 2OH^- \quad (5)$$

The microstructure of Mg alloy significantly influences its corrosion behavior. As discussed in section 4.1, the addition of Ce visibly refined the grain size of α-Mg, caused the formation of Al_4Ce phase, reduced the volume fraction of $Mg_{17}Al_{12}$ and increased the solid solution of Sn in α-Mg. Generally speaking, grain boundaries that encompass crystal defects, including dislocations and vacancies, can act as active sites, which are conducive to the nucleation and growth of passive films[43]. When Mg alloys are exposed to a corrosive environment, the atoms located at the grain boundaries have a higher probability of reacting with the medium in the environment, thereby forming a dense passive film. For example, at the initial stage of corrosion, components of the passive film, such as Mg oxides or hydroxides, are preferentially formed at the grain boundaries and can isolate the Mg alloy matrix from the external corrosive medium, thus enhancing the corrosion resistance of the Mg alloy[48]. Grain boundaries can impede the propagation of cracks, associated with the slow diffusion rates of the corrosive medium at the grain boundaries because the different chemical composition and atomic structure at the grain boundaries, which differ from those inside the grains, result in such slow diffusion, thereby slowing down the overall corrosion rate of the Mg alloy[43,50]. According to the principles of materials science, refining grains implies that there will be more grain boundaries in the alloy. For the alloys under study, the grain size of α-Mg changes from 230 μm in the base alloy to 140 μm in the 3# alloy, and the refined α-Mg has a positive influence on the enhancement of the corrosion resistance (CR). The secondary phases ($Mg_{17}Al_{12}$, Al_4Ce and Mg_2Sn) in as-cast alloys exhibit nobler potentials than Mg[3]. A larger electric potential difference between these secondary phases (as cathodes) and α-Mg (as the anode) results in more Mg being consumed during immersion in NaCl solution, leading to higher corrosion rates. Liu et al.[17] observed that both Al_4Ce and $Mg_{17}Al_{12}$, considered as cathodes, have more positive Volta potentials than α-Mg in AZ91–*x*Ce alloys immersed in NaCl solution. This indicates the formation of Al_4Ce reduces the micro-galvanic corrosion between $Mg_{17}Al_{12}$ and α-Mg, thereby enhancing the CR in Ce-added alloys. Furthermore, the quality of the corrosion product film likewise gives a strong influence on the CR of alloys as reported in Ce-added AZ91D and AM60 alloys[17,18]. In contrast with base alloy, the corrosion product film in Ce-added alloys is relatively compact (Figure 13), providing better protection and reducing the corrosion rate. Thus, the superior CR is primarily owing to the refined microstructure and a low volume fraction of discontinuous $Mg_{17}Al_{12}$ phase in these alloys with an appropriate addition of Ce[15].

Note that, the CR of 4# alloy becomes weak compared to that of 3# alloy. The reason is related to the coarse Al_4Ce phase distributed along the grain boundary and interior of the grains (Figure 3). During corrosion in NaCl solution, these coarse phases acted as cathode phases against Mg matrix as the anode phases, which possibly formed the "big cathode, small anode" in local regions for 4#, resulted in the somewhat increased corrosion rate, similar to the detrimental impact of high Y content (2 wt. %) in AZ91 alloy[57].

5. Conclusions

The microstructures, phase compositions, tensile properties, and corrosion behaviors of as-cast Mg–7.5Al–2Sn–1Zn (wt. %) alloys with and without Ce additions (0.5, 1.0 and 2.0 wt. %) have been studied. The key findings are summarized as follows:

Minor additions of Ce in Mg–7.5Al–2Sn–1Zn (wt. %) alloys significantly refined the microstructure, reducing the average grain size of α-Mg from 233 μm in the base alloy to 140 μm in the 1.0 wt.% Ce-added alloy. This refinement was accompanied by the promotion of the Al_4Ce phase and a reduction in the volume fraction of the $Mg_{17}Al_{12}$ phase as the Ce addition increased. Tensile properties of the base alloy were markedly improved at both room temperature and 175 °C with minor Ce addition. The 1.0 wt. % Ce alloy exhibited superior tensile properties, achieving a UTS of ~237 MPa, YS of ~98 MPa and elongation to failure (E_f) of ~16.7% at room temperature. These improvements represent increases of ~22%, ~17% and ~52%, respectively, compared to the base alloy. The enhancements are attributed to solid solution strengthening, grain refinement strengthening and the influence of secondary phases. Corrosion resistance of the alloys was significantly enhanced with Ce addition. The corrosion rate decreased from 8.4 mm/yr in the base alloy to 1.8 mm/yr in the 1.0 wt. % Ce alloy, as determined by immersion tests. This improvement is attributed to the modified microstructure resulting from Ce addition, which was confirmed by polarization curves and surface morphology analysis of the immersed samples.

6. Acknowledgments

This work was supported by the Jilin Provincial Department of Science and Technology, project number [20220201128GX].

7. References

1. Joost WJ, Krajewski PE. Towards magnesium alloys for high-volume automotive applications. Scr Mater. 2017;128:107-12. http://doi.org/10.1016/j.scriptamat.2016.07.035.
2. Ogawa Y, Ando D, Sutou Y, Koike J. A lightweight shape-memory magnesium alloy. Science. 2016;353(6297):368-70. http://doi.org/10.1126/science.aaf6524.
3. Wang XJ, Xu DK, Wu RZ, Chen XB, Peng QM, Jin L, et al. What is going on in magnesium alloys? J Mater Sci Technol. 2018;34(2):245-7. http://doi.org/10.1016/j.jmst.2017.07.019.
4. Zhang S-Y, Wang C, Zhao L-Q, Ma P-K, Song J-W, Xu J, et al. Superplastic deformation behavior of rolled Mg-8Al-2Sn and Mg-8Al-1Sn-1Zn alloys at high temperatures. Materials. 2020;13(5):1074. http://doi.org/10.3390/ma13051074.
5. Atrens A, Chen X, Shi Z. Mg corrosion: recent progress. Corros Mater Degrad. 2022;3(4):566-97. http://doi.org/10.3390/cmd3040031.
6. Luo AA, Fu P, Peng L, Kang X, Li Z, Zhu T. Solidification microstructure and mechanical properties of cast Magnesium-Aluminum-Tin Alloys. Metall Mater Trans, A Phys Metall Mater Sci. 2012;43A(1):360-8. http://doi.org/10.1007/s11661-011-0820-y.
7. Zhang SY, Wang C, Ning H, Wang T, Zhang CC, Yang Z-Z, et al. Relieving segregation in twin-roll cast Mg–8Al–2Sn–1Zn alloys via controlled rolling. J Magnes Alloy. 2021;1(1):254-65. http://doi.org/10.1016/j.jma.2020.04.007.
8. Shi X, Li Y, Zeng X, Liu Y, Chen B, Lu J, et al. Deformation mechanism and dynamic precipitation in a Mg-7Al-2Sn alloy processed by surface mechanical attrition treatment. J Mater Sci Technol. 2019;35(7):1473-8. http://doi.org/10.1016/j.jmst.2019.02.007.

9. Mendis CL, Bettles CJ, Gibson MA, Hutchinson CR. An enhanced age hardening response in Mg-Sn base alloys containing Zn. Mater Sci Eng A. 2006;435–436:163-71. http://doi.org/10.1016/j.msea.2006.07.090.
10. Park SH, Jung JG, Kim YM, You BS. A new high-strength extruded Mg-8Al-4Sn-2Zn alloy. Mater Lett. 2015;139:35-8. http://doi.org/10.1016/j.matlet.2014.10.033.
11. Liu C, Chen H, He C, Zhang Y, Nie JF. Effects of Zn additions on the microstructure and hardness of Mg-9Al-6Sn alloy. Mater Charact. 2016;113:214-21. http://doi.org/10.1016/j.matchar.2016.01.021.
12. Ma CY, Guan XF, Sun L, Liu GJ. Microstructure and mechanical properties of modified Mg-8Al-2Sn alloys using Zn addition combined with artificial aging treatment. Mater Sci Eng A. 2022;831:142278. http://doi.org/10.1016/j.msea.2021.142278.
13. Wu L, Li H. Effect of selective oxidation on corrosion behavior of Mg–Gd–Y–Zn–Zr alloy. Corros Sci. 2018;142:238-48. http://doi.org/10.1016/j.corsci.2018.07.026.
14. Yang M, Cheng L, Pan F. Comparison about effects of Ce, Sn and Gd additions on as-cast microstructure and mechanical properties of Mg-3.8Zn-2.2Ca (wt%) magnesium alloy. J Mater Sci. 2009;44(17):4577-86. http://doi.org/10.1007/s10853-009-3696-0.
15. Mingo B, Arrabal R, Mohedano M, Mendis CL, Olmo R, et al. Corrosion of Mg-9Al alloy with minor alloying elements (Mn, Nd, Ca, Y and Sn). Mater Des. 2017;130:48-58. http://doi.org/10.1016/j.matdes.2017.05.048.
16. Zhang J, Zhang D, Tian Z, Wang J, Liu K, Lu H, et al. Microstructures, tensile properties and corrosion behavior of die-cast Mg-4Al-base alloys containing La and/or Ce. Mater Sci Eng A. 2008;489(1-2):113-9. http://doi.org/10.1016/j.msea.2007.12.024.
17. Liu W, Cao F, Zhong L, Zheng L, Jia B, Zhang Z, et al. Influence of rare earth element Ce and La addition on corrosion behavior of AZ91 magnesium alloy. Mater Corros. 2009;60(10):795-803. http://doi.org/10.1002/maco.200805179.
18. Liu WJ, Cao F, Chang L, Zhang Z, Zhang JQ. Effect of rare Earth elements Ce and La on corrosion behavior of AM60 magnesium alloys. Corros Sci. 2009;51(6):1334-43. http://doi.org/10.1016/j.corsci.2009.03.018.
19. Kim BH, Kimura H, Park YH, Park IM. The effect of cerium on microstructures and mechanical properties of Mg-4Al-2Sn-1Ca alloy. Mater Trans. 2010;51(7):1346-9. http://doi.org/10.2320/matertrans.M2010042.
20. Kutaitseva AI, Timonova MA. Corrosion resistance of magnesium alloy sheet. Metal Sci Heat Treat. 1960;2(8):453-6. http://doi.org/10.1007/BF00656478.
21. Wang X, Zeng X, Yao S, Wu G, Lai Y. The corrosion behavior of Ce-implanted magnesium alloys. Mater Charact. 2008;59(5):618-23. http://doi.org/10.1016/j.matchar.2007.05.006.
22. Guan S, Wang PY, Wang TH, Wang CG, Liu GJ, Zhu YF. Microstructure and mechanical properties of high-pressure die-casting Mg–Al–RE alloys with minor Ca addition. Materials. 2025;18(2):231. http://doi.org/10.3390/ma18020231.
23. Esmaily M, Svensson JE, Fajardo S, Birbilis N, Frankel GS, Virtanen S, et al. Fundamentals and advances in magnesium alloy corrosion. Prog Mater Sci. 2017;89:92-193. http://doi.org/10.1016/j.pmatsci.2017.04.011.
24. Rosalbino F, Angelini E, Negri SD, Saccone A, Delfino S. Electrochemical behaviour assessment of novel Mg-rich Mg-Al-RE alloys (RE=Ce, Er). Intermetallics. 2006;14(12):1487-92. http://doi.org/10.1016/j.intermet.2006.01.056.
25. Leleu S, Rives B, Bour J, Causse N, Pébère N. On the stability of the oxides film formed on a magnesium alloy containing rare-earth elements. Electrochim Acta. 2018;290:586-94. http://doi.org/10.1016/j.electacta.2018.08.093.
26. Song YL, Liu YH, Wang SH, Yu SR, Zhu XY. Effect of cerium addition on microstructure and corrosion resistance of die cast AZ91 magnesium alloy. Mater Corros. 2007;58(3):189-92. http://doi.org/10.1002/maco.200603988.
27. Zhao MC, Liu M, Song GL, Atrens A. Influence of microstructure on corrosion of as-cast ZE41. Adv Eng Mater. 2008;10(1-2):104-11. http://doi.org/10.1002/adem.200700246.
28. Wang HY, Rong J, Liu GJ, Zha M, Wang C, Luo D, et al. Effects of Zn on the microstructure and tensile properties of as-extruded Mg-8Al-2Sn alloy. Mater Sci Eng A. 2017;698:249-55. http://doi.org/10.1016/j.msea.2017.05.055.
29. Liu W, Cao F, Chen A, Chang L, Zhang J, Cao C. Corrosion behaviour of AM60 magnesium alloys containing Ce or La under thin electrolyte layers. Part 1: microstructural characterization and electrochemical behavior. Corros Sci. 2010;52(2):627-38. http://doi.org/10.1016/j.corsci.2009.10.031.
30. Manivannan S, Kannan S, Babu SPK. Effect of cerium addition on corrosion behaviour of AZ61 +*x*Ce alloy under salt spray test. Alex Eng J. 2016;55(1):663-71. http://doi.org/10.1016/j.aej.2015.10.010.
31. Bai J, Sun Y, Ding S, Xue F, Wang L. Microstructure and tensile properties of AE42 base magnesium alloys with calcium addition. J Southwest Univ. 2004;20:43-8.
32. Wan XF, Sun YS, Xue F, Bai J, Tao WJ. Microstructure and mechanical properties of Mg-12Zn-4Al-0.3Mn alloy containing Sr and Ca. Chin Shu Hsueh Pao. 2009;45:585-91.
33. Kim JM, Park BK, Jun JH, Shin K, Kim KT, Jung WJ. Microstructure and heat resistance of Mg-Al-Zn alloys containing metastable phase. Mater Sci Eng A. 2007;449-451:326-9. http://doi.org/10.1016/j.msea.2006.02.447.
34. Nie ZK. Effect of Ca on microstructure and properties of AZ91-0.4Ce-xCa magnesium alloy. Chongqing: Chongqing University; 2022.
35. Bai J, Sun Y, Xue F, Xue S, Qiang J, Zhu T. Effect of Al contents on microstructures, tensile and creep properties of Mg-Al-Sr-Ca alloy. J Alloys Compd. 2007;437(1-2):247-53. http://doi.org/10.1016/j.jallcom.2006.07.096.
36. Zhang WQ, Xiao WL, Wang F, Ma CL. Develop ent of heat resistant Mg-Zn-Al-base magnesium alloys by addition of La and Ca: microstructure and tensile properties. J Alloys Compd. 2016;684:8-14. http://doi.org/10.1016/j.jallcom.2016.05.137.
37. Wang F, Hu T, Zhang Y, Xiao W, Ma C. Effects of Al and Zn contents on the microstructure and mechanical properties of Mg-Al-Zn-Ca magnesium alloys. Mater Sci Eng A. 2017;704:57-65. http://doi.org/10.1016/j.msea.2017.07.060.
38. Yan JL, Sun YS, Xue F, Xue S, Tao WJ. Microstructure and mechanical properties in cast magnesium–neodymium binary alloys. Mater Sci Eng A. 2008;476(1-2):366-71. http://doi.org/10.1016/j.msea.2007.05.058.
39. Gan JX, Zhang F, Han XZ, Liu CM. Effects of mischmetal on microstructure and mechanical properties of AZ80 magnesium alloy. Ord Mater Sci Eng. 2015;38:81-4. http://doi.org/10.14024/j.cnki.1004-244x.2015.01.022
40. Mao GB, Liu Q. Influence of Sr addition on microstructure and mechanical properties of AZ91 magnesium alloy. Foundry. 2010;59:614-7.
41. Kim JM, Park BK, Shin K, Jun JH, Kim KT, Jung WJ. Development of Mg-Al-Zn base diecasting alloys for elevated temperature applications. Mater Sci Forum. 2005;479:525-8. http://doi.org/10.4028/www.scientific.net/MSF.475-479.525.
42. Fan JP, Xu BS, Wang SB, Liu L, Feng ZY. Effect of Sr/Al ratio on microstructure and properties of Mg-Al-Sr alloy. Rare Met Mater Eng. 2012;41(10):1721-4. http://doi.org/10.1016/S1875-5372(13)60013-2.
43. Song G. Corrosion of magnesium alloys. Cambridge: Woodhead Publishing Limited; 2011. http://doi.org/10.1533/9780857091413.
44. Zhao MC, Schmutz P, Brunner S, Liu M, Song GL, Atrens A. An exploratory study of the corrosion of Mg alloys during interrupted salt spray testing. Corros Sci. 2009;51(6):1277-92. http://doi.org/10.1016/j.corsci.2009.03.014.

45. Kim J, Nguyen HN, You BS, Kim YM. Effect of Y addition on removal of Fe impurity from magnesium alloys. Scr Mater. 2019;162:355-60. http://doi.org/10.1016/j.scriptamat.2018.11.046.
46. Feng JW, Li HN, Deng KK, Fernandez C, Zhang QR, Peng QM. Unique corrosion resistance of ultrahigh pressure Mg-25Al binary alloys. Corros Sci. 2018;143:229-39. http://doi.org/10.1016/j.corsci.2018.08.013.
47. Liu Q, Ma QX, Chen GQ, Cao X, Zhang S, Pan JL, et al. Enhanced corrosion resistance of AZ91 magnesium alloy through refinement and homogenization of surface microstructure by friction stir processing. Corros Sci. 2018;138:284-96. http://doi.org/10.1016/j.corsci.2018.04.028.
48. Xiang Q, Jiang B, Zhang YX, Chen XB, Song JF, Xu JY, et al. Effect of rolling-induced microstructure on corrosion behaviour of an as-extruded Mg-5Li-1Al alloy sheet. Corros Sci. 2017;119:14-22. http://doi.org/10.1016/j.corsci.2017.02.009.
49. Turan ME, Sun Y, Akgul Y, Turen Y, Ahlatci H. The effect of GNPs on wear and corrosion behaviors of pure magnesium. J Alloys Compd. 2017;724:14-23. http://doi.org/10.1016/j.jallcom.2017.07.022.
50. Arrabal R, Pardo A, Merino MC, Mohedano M, Casajús P, Paucar K, et al. Effect of Nd on the corrosion behaviour of AM50 and AZ91D magnesium alloys in 3.5 wt.% NaCl solution. Corros Sci. 2012;55:301-12. http://doi.org/10.1016/j.corsci.2011.10.033.
51. Maltseva A, Shkirskiy V, Lefèvre G, Volovitch P. Effect of pH on $Mg(OH)_2$ film evolution on corroding Mg by in situ kinetic Raman mapping (KRM). Corros Sci. 2019;153:272-82. http://doi.org/10.1016/j.corsci.2019.03.024.
52. Jia R, Yu S, Li D, Zhang T, Wang F, Zhong C. Study on the effect of mischmetal (La, Ce) on the micro-galvanic corrosion of AZ91 alloy using multiscale methods. J Alloys Compd. 2019;778:427-38. http://doi.org/10.1016/j.jallcom.2018.11.030.
53. Liu SF, Li B, Wang XH, Su W, Han H. Refinement effect of cerium, calcium and strontium in AZ91 magnesium alloy. J Mater Process Technol. 2009;209(8):3999-4004. http://doi.org/10.1016/j.jmatprotec.2008.09.020.
54. Kim S-H, Park SH. Influence of Ce addition and homogenization temperature on microstructural evolution and mechanical properties of extruded Mg-Sn-Al-Zn alloy. Mater Sci Eng A. 2016;676:232-40. http://doi.org/10.1016/j.msea.2016.08.093.
55. Grimm M, Lohmüller A, Singer RF, Virtanen S. Influence of the microstructure on the corrosion behaviour of cast Mg-Al alloys. Corros Sci. 2019;155:195-208. http://doi.org/10.1016/j.corsci.2019.04.024.
56. Natarajan AR, Van Der Ven A. A unified description of ordering in HCP Mg-RE alloys. Acta Mater. 2017;124:620-32. http://doi.org/10.1016/j.actamat.2016.10.057.
57. Luo TJ, Yang YS, Li YJ, Dong XG. Influence of rare earth Y on the corrosion behavior of as-cast AZ91 alloy. Electrochim Acta. 2009;54(26):6433-7. http://doi.org/10.1016/j.electacta.2009.06.023.

Data Availability

The comprehensive dataset that underpins the findings of this study can be obtained by submitting a request to the corresponding author, [Ting Wang].

However, this dataset is not publicly released. The rationale behind this is that the data presented in this article are an integral part of an ongoing research initiative. Revealing the data prematurely at this juncture has the potential to impede the publication of subsequent research outcomes.

We deeply value your understanding of this situation. We are firmly committed to making the full dataset accessible at a suitable time in the future. For those interested in accessing the dataset, they can either wait for the appropriate time or submit a request directly to the corresponding author.